Invited Papers

Spatially resolved thermometry during laser ablation in tissues: Distributed and quasi-distributed fiber optic-based sensing

Federica Morra[a], Martina De Landro[a], Sanzhar Korganbayev[a], Alexey Wolf[b], Alexander Dostovalov[b], Alfredo Cigada[a], Paola Saccomandi[a,*]

[a] Department of Mechanical Engineering, Politecnico di Milano, Milan, Italy
[b] Laboratory of Fiber Optics, Institute of Automation and Electrometry SB RAS, Novosibirsk, Russia

ARTICLE INFO

ABSTRACT

This work assesses quasi-distributed Fiber Bragg Gratings (FBGs) and Rayleigh scattering-based distributed sensing for accurate and millimeter resolved thermometry in media undergoing laser ablation. Mono-, two- and three-dimensional temperature measurements were performed with a network of 1 mm-long FBGs in 10-25-40-FBGs-arrays and distributed-sensing fiber with gauge lengths (GL) of 5.2 and 1.3 mm. Results confirm that the lower the spatial resolution of the sensors, the highest the root mean square error (RMSE) and temperature underestimation with respect to reference sensors (25-FBGs array). Compared to 1 mm-long FBGs, distributed sensing with 5.2 mm GL provided RMSE > 7 °C and underestimation > 16 °C in agar-gel phantom. Signal-to-noise ratio over time and temperature standard deviation over temperature show better performances of FBGs over distributed sensors. Indeed, any improvement of spatial resolution for distributed sensors determines an increase of noise in the signal. The three-dimensional measurement performed with 420 FBGs with 1 mm-sensing length demonstrated the spatial and thermal gradient occurring in the pancreas undergoing LA, reaching 28 °C over 5 mm. Millimeter-resolved FBGs proved to be effective for accurate thermometry in laser irradiated tissues, and potentially usable in clinical applications.

1. Introduction

Interventional oncology is a new and fast-evolving branch of interventional radiology, which relies on advanced tools and precise image-based guidance to target and treat tumours [1]. Interventional oncologists adopt minimally invasive and energy-based techniques for the treatment of localized tumors, by inserting a needle or a catheter through a small percutaneous incision to access the affected organ. Energy-based techniques, such as radiofrequency, microwave, and laser ablation are gaining rising acceptance and recognition in the clinical applications [2]. These minimally invasive procedures have demonstrated substantial edges over surgery, such as the reduction of physical impact, recovery time and short- and long-term adverse events. They stand as the potential solutions for some malignancies, such as the non-respectable liver metastases from colorectal cancer which are resistant to systemic chemotherapy [3,4]. Additionally, in conjunction with eco-endoscopic guidance, thermal ablation was proved to be beneficial to treat malignancies in difficult locations, like pancreas [5–7]. For the minimally invasive thermal ablation therapies, the interaction between an electromagnetic wave with the biological tissue aims at producing a

therapeutic increase of the tumor mass temperature beyond the cyto-toxic level. Thermal ablation operates at a temperature in the range of 50 to 100 °C, or even higher, with exposure times between 1 and 30 min [8]. Laser ablation (LA) is a thermal ablation technique introduced in the 1980 s in the ophthalmologic field and for the treatment of some gastrointestinal and brain tumors [9,10]. Its main feature is the delivery of energy through small optical fibers (0.3–0.6 mm), in both contact and contactless fashions [11,12]. The fiber tip can be manufactured in order to optimize the irradiation pattern to the shape and size of the target [11,13]. The adequate absorption and scattering properties of biological media within the so-called therapeutic window favour the use of laser in the near infrared range, mostly comprised between 800 and 1064 nm [9,14]. The small fibers delivering the laser light into the targets, along with the complex phenomenon of the light-tissue inter-action, contribute to produce a high spatial thermal gradient evolving in time that could exceed 50 °C/mm in proximity of the applicator tip [15]. Thus, the main temperature effects of the thermal ablation tech-niques, are the carbonization and necrosis of the central region of the target, surrounded by a region of irreversible (for T > 50 °C and sufficient exposure time) and then sublethal and reversible (T < 45 °C)

---

thermal damage [16]. The extension of the irreversible and reversible regions depends on the penetration of the light inside the tissue and on the heat conduction. Hence, it emerges the importance of having a measurement system for monitoring the tissue temperature with enough accuracy in terms of both temperature and space. These properties will guarantee a safe clinical procedure and a real-time control of the delivered energy. The feature of sub-centimeter spatial resolution possessed by several fiber optic sensors has allowed several applications for temperature monitoring in biological media. Fiber Bragg gratings (FBG), both uniform and chirped, are used for different goals, such as tumor detection [17], and thermal ablation monitoring [18–21]. Uniform FBGs allow for a typical spatial resolution from 1 grating/cm to 1 grating/mm [22,23]. Linear chirped FBGs (LCFBGs) behave as a continuous set of FBGs, thus the spatial resolution can theoretically achieve and outdo the order of 100 sensor/1 mm [24,25]. However, the complex estimation of parameters required to assess the temperature pattern from the spectrum modulation still limits the use of LCFBG to applications where the thermal pattern has a known trend [19,26]. For FBGs, the proper choice of the optimal spatial resolution depends to sensor length and relative distance, and can significantly affect the measurement performances during LA [21,27]. Some works have also investigated optical frequency domain reflectometry (OFDR) based on Rayleigh scattering, as distributed sensing approach for temperature measurements [19,28,29]. Distributed fiber optic sensing relies on the principle that a single optical fiber as a specific scattering signature based on the material properties, which are also temperature-dependent. Theoretically, these systems allow for infinite sensing points for a given length. However, commercially available devices limit the selectable spatial resolution to a few millimeters, which is inversely proportional to the sampling frequency and instrumental accuracy. Compared to Rayleigh-based technology, the total sensing length of FBG technology is limited by the bandwidth of the interrogation system and multiplexing capacity. On the other hand, FBGs-based technology can achieve high signal-to-noise ratio since it has good back-scattering light coupling efficiency [22].

Whereas several studies point out the impact of the spatial resolution for accurate thermometry during thermal therapies, a direct comparison among different sensing techniques is still needed. Thus, this work aims at evaluating and comparing quasi-distributed FBG sensing and distributed sensing performed with OFDR based on Rayleigh scattering. The temperature measurements were acquired from the sensors in two different approaches and for two tissue phantoms: i) contactless ablation of an agar gel phantom was evaluated with mono-dimensional (1D) and superficial (2D) temperature measurements with a network of FBGs and distributed sensors; ii) contact ablation of an agar gel phantom and of an *ex vivo* pancreas tissue was assessed with 1D and volumetric (3D) temperature monitoring with FBGs. The performances of the two measurement systems were evaluated in terms of root means squared error, temperature differences and signa-to-noise ratio, and then results were compared.

2. Experimental instrumentation

2.1. FBG-based sensing

An FBG is a wavelength-dependent reflector, resulting from a periodic modulation of the refraction index along the fiber core. It reflects a narrow portion of the spectrum, centered around a specific Bragg wavelength, λ_B, that is proportional to the distance between two regions with high refractive indices (the grating period Λ) [30]:

$$\lambda_B = 2n_{eff}\Lambda \tag{1}$$

The material of the fiber and, as a result, grating planes are affected by temperature perturbations, that alter the grating period and the related λ_B. Therefore, tracking of λ_B allows monitoring of the temperature changes along the grating, according to Eq. (2):

$$\frac{\Delta\lambda_B}{\lambda_B} = \frac{\lambda_{B,\Delta T} - \lambda_{B,initial}}{\lambda_B} = \alpha\Delta T \tag{2}$$

where α ($°C^{-1}$) is the thermal sensitivity of the grating.

In addition, a chain of FBGs along one fiber, the so-called FBG array, can provide quasi-distributed sensing if each FBG has a different λ_B. As a result, an FBG array provides a discrete temperature map, whereas each FBG acts as a sensing point. The finite number of gratings and the Bragg wavelength resolution between adjacent FBGs are related to the maximum allowed bandwidth which, in turn, limits the sensing length.

Three FBG configurations were employed: commercially available arrays of 10 FBGs (FiSens GmbH, Braunschweig, Germany), and custom-made arrays of 25 FBGs and 40 FBGs, respectively. All the arrays were inscribed in a single-mode optical fiber using the femtosecond point-by-point writing technology [31]. In order to discriminate FBGs in the 1460–1620 nm spectral region of the Micron Optics si255 interrogation unit (*Micron Optics*, Atlanta, USA) the periods of FBG and related Bragg wavelengths were changed along the array during inscription. All arrays have polyimide coating which provides higher temperature resistance (up to 400 °C in short term operation and at 300 °C in continuous operation) in comparison with acrylate coating (up to 85 °C) [31,32]. The polyimide coating is also characterized by low thermal conductivity (i.e., 0.12 $W·m^{-1}·K^{-1}$), which allows for a reduced thermal effect due to heat transfer between adjacent gratings. The arrays of 10 FBGs have a 1 mm grating length and a 1 mm distance between grating edges. The arrays of 25 FBGs and 40 FBGs have grating lengths of a 0.9 mm and 1.19 mm, respectively, and the edge-to-edge distances between gratings equal to 0.1 mm and 0.01 mm, correspondingly.

2.2. Distributed sensing

For distributed sensing, a commercially available LUNA ODiSI-B measurement system (LunaInc, Blacksburg, VA, USA) based on Rayleigh scattering was used. Rayleigh scattering phenomenon occurs when a part of the input light is reflected from the microstructural fluctuations in the refractive index profile along the fiber. The pattern of these fluctuations is individual for every fiber after manufacturing and alters only due to external perturbations such as temperature, strain, and humidity [33]. Therefore, each fiber segment has its own backscatter spectrum, that shifts according to temperature or strain applied to this segment. As a result, similarly to the Bragg wavelength shift of FBGs, each segment acts as a sensing point. The size of this segment, also called the gauge length, affects both the signal-to-noise ratio and the resolution of the spectral shift measurements. Longer gauge lengths, indeed, cause an increase in the accuracy but also result in a decrease of the spatial resolution. Thus, Rayleigh based measurement has a trade-off between accuracy and the spatial resolution of the measurement [33,34].

The LUNA ODiSI-B is capable to provide both static and dynamic measurements along lengths up to 20 m at a rate up to 250 Hz. It also allows a 50% overlapping of 5.20 mm and 1.30 mm gauge lengths, resulting in 2.61 mm and 0.65 mm spatial resolution, respectively [34]. Measurements were performed in standard and high-resolution modes (2.61 and 0.65 mm spatial resolution, respectively). The acrylate-coated standard single-mode fiber (Corning SMF-28®, Corning Incorporated, Corning, NY, USA) and polyimide-coated High-Definition fiber optic sensor (HD-FOS) (LunaInc, Blacksburg, VA, USA) were used with LUNA ODiSI-B. Static sensitivity for the commercial HD-FOS was provided by the manufacturer [35].

Temperature sensitivity coefficients of the FBG arrays and Corning SMF-28 were obtained in a certified thermostatic calibrator (Giussani Quartz, operative field from −40 °C to 125 °C) in the temperature range 20 °C−125 °C, with a step of 10 °C. A PT100 thermistor (±0.15 °C accuracy) was used as a reference sensor. The reference values were recorded with the Delta Ohm HD2178.2 system. The acquisition of
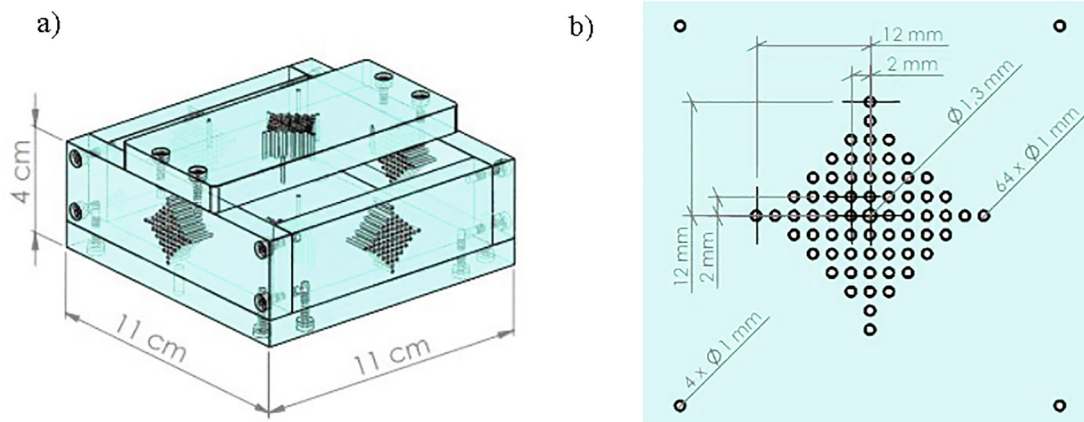
Fig. 1. a) Plexiglass placement system, external dimension $11 \times 11 \times 4$ cm^3; b) dimensions for the central patterns.

FBGs' signal was performed by Micron Optics HYPERION si255, while the signal of the Corning SMF-28 was detected by the LUNA ODiSI-B system. The static sensitivities α for the FBGs are: (7.30 ± 0.01) $\cdot 10^{-6}$ °C^{-1} for the 10-FBGs array, $(7.43 \pm 0.01) \cdot 10^{-6}$ °C^{-1} for the 25-FBGs array, $(7.63 \pm 0.01) \cdot 10^{-6}$ °C^{-1} for the 40-FBGs array. The static sensitivity of the Corning SMF-28 is -10.70 ± 0.05 pm·°C^{-1}.

2.3. Laser and sensors positioning systems

Laser ablation was performed by a diode laser working at $\lambda = 1064$ nm (LuOcean Mini 4, Lumics, Berlin, Germany). The laser light was delivered by two different optical fibers: *i)* in the 2D experiments, a 440 μm diameter optical fiber with a numerical aperture equal to 0.22 was used to perform a contactless ablation of the agarose surface using the collimator connected to the applicator's tip; *ii)* in the 3D experiments, a 300 μm diameter quartz fiber was, instead, inserted in both agarose phantom and pancreas targets for performing a deep contact ablation.

A plexiglass box was *ad hoc* designed to perform laser ablation experiments (Fig. 1). The setup allows accurate positioning of the laser applicator and the fiber sensors inside the phantom inserted in the box. Sixty-four holes with 1 mm-diameter have been designed to offer a wide range of possible arrangements for the sensors with a minimum distance of 2 mm from the laser applicator (central hole, 1.3 mm-diameter). The reason for such a small distance can be found in the high-temperature gradient which characterizes heat transfer in soft tissues undergoing laser irradiation [15].

2.4. Tissue phantom

Laser ablation was performed in: *i)* 3% agar gel phantom, which has demonstrated to have similar thermal properties to that of soft tissues [36]. The homogeneity of the phantom makes it a suitable base for a preliminary comparison of the fiber optic sensors performances. The gel was prepared by adding 30 g of agarose in 1 l of milli-Q water. The solution was then heated and blended until the agarose was completely dissolved. Afterward, the solution was poured directly in the plexiglass box and then stored at 4 °C for the solidification and for preventing the gel from drying out; *ii)* *ex vivo* porcine pancreas, to include the non-homogeneous properties of a real tissue and mimic a potential pre-clinical scenario. The tissue was obtained from a local butcher the same day of the experiment and stored at 4 °C until the experiment was carried out. Some metrological bench-tests have been already proposed to assess the performances of FBGs for temperature monitoring in biological tissues [24,37]. In this work, the choice to tests the fiber optic sensing systems directly on tissue-mimicking phantoms is motivated by the need of realizing testing conditions which are as close as possible to the real application.

3. Contactless ablation of the agarose phantom

The aim of these experiments is to compare temperature measurements provided by the 25-FBGs arrays, 10-FBGs arrays and LUNA ODiSI-B (Corning SMF-28 and HD-FOS) sensors during a contactless ablation of an agarose phantom. Temperature measured by the 25-FBGs arrays was used as a control because of the sensor's higher spatial resolution. Two parameters were chosen to quantify the temperature reconstruction error: peak difference (PD), defined as the difference between maximum temperatures measured by the 25-FBGs arrays and by the other sensors, and the root means squared error (RMSE) between measured and control spatial temperature profiles. The performances of the sensors were also evaluated in terms of signal-to-noise ratio (SNR) over time and temperature standard deviation (STD) as a function of measured temperature change.

3.1. Material and methods

Contactless ablation experiments involved the use of 5 triplets of fiber optic sensors, each triplet consisted of: the 25-FBGs array, the 10-FBGs array and LUNA ODiSI-B sensor.

The custom-made box was used to house the agar gen, place the sensors on its surface and control the relative distance among the triplets (Fig. 2a). Passing through the holes in the opposite wall sides, grooves at 2 mm distance were made on the agar phantom using 1 mm-diameter needles (Fig. 2b). Distance between the laser beam collimator and the agar gel surface was 4 cm, the 10 mm-diameter laser spot was focused on the central triplet. In order to avoid the agar gel melting, the laser power was tuned to obtain the maximum temperature measured by the control sensor equal to 30 ± 1 °C in 60 s of irradiation. Each experiment was repeated three times. Two types of analysis were carried out:

1) 1D comparison performed on the central triplet, where the highest spatial temperature gradient is present and better performances are needed for an accurate temperature map [27]. FBGs were compared with: a) Corning SMF-28 with GL = 5.2 mm and 1.3 mm GL (2.61 and 0.65 mm spatial resolution, respectively), and b) Luna HD-FOS with GL = 5.2 mm and 1.3 mm (2.61 and 0.65 mm spatial resolution, respectively).
2) 2D map reconstruction with one Corning SMF-28, which was curved in order to obtain 5 segments overlapped with the FBG arrays (Fig. 2b). Temperature profiles measured along these segments allow to reconstruct a 2D temperature map, that can be compared with a 2D map obtained by the FBG sensors.
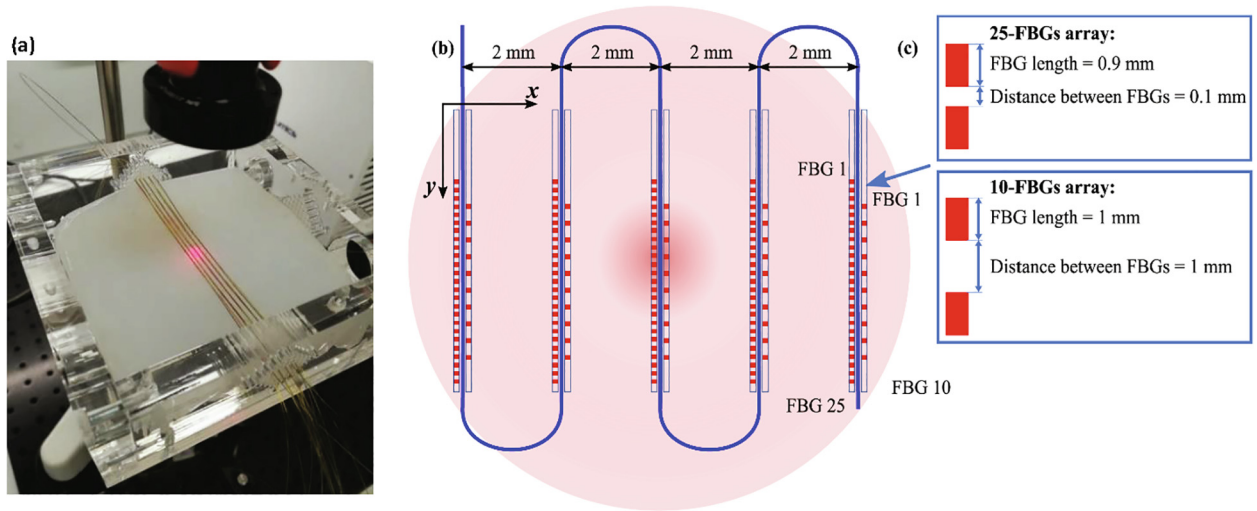
Fig. 2. Experimental setup: a) 5 triplets of fiber sensors placed on the agarose surface inside the box at a 2 mm distance from each other. The laser spot is focused on the central triplet; b) Schematic representation; c) Zoom-in of the schematic illustrating spatial characteristics of the gratings.
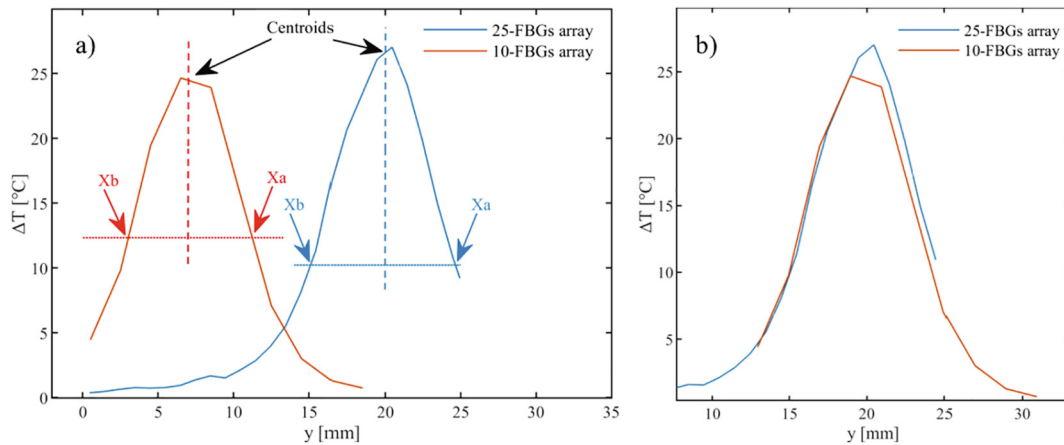

Fig. 3. Temperature change *vs.* distance along the sensor: a) Centroid method implemented for aligning 25-FBGs and 10-FBGs arrays temperature distributions; b) final alignment obtained by shifting 10-FBGs array centroid respect to the 25-FBGs array one. The same approach is used for LUNA ODiSI-B measurements alignment.

A comparison among the sensors along one single dimension was initially performed. Beyond temporal alignment for the post-synchronization of data acquired by Luna and Micron Optic systems, also spatial alignment was needed (Fig. 2b). Indeed, accurate alignment of the sensors along y axis was not manually achievable due to different resolutions and short sensing lengths of the sensors in each triplet. The spatial alignment was obtained with the centroid method (Fig. 3). Centroid positions X_{centr} are computed as shown in Eq. (3):

$$X_{centr} = \frac{X_a + X_b}{2}$$

(3)

where X_a and X_b are coordinates of the halves of the maximum temperature.

The aligned temperature curves were compared using the 25-FBGs array measurement as a reference. RMSE and PD were evaluated between the temperature curves acquired at three time-instants within 15 s the end of irradiation, when the maximum temperature is reached (Fig. 4).

The same temporal and spatial alignments were also performed for the 2D temperature map reconstruction. The five triplets were also aligned along y axis, and the obtained temperature maps were reconstructed and compared.

In addition, the Signal to Noise Ratio (SNR) and the Temperature Standard Deviation (STD) was estimated for each sensor. SNR was

obtained with the Eq. (4):

$$SNR = 20\log_{10}\left(\frac{RMS(T)}{RMS(N)}\right)$$

(4)

where RMS is the root mean square function, T is the measured temperature signal and N is the signal noise. The noise was computed by acquiring the temperature signal provided by each sensor at room temperature, within a window of 20 s.

3.2. Results and discussion

The temperature evolution in time measured by the 25-FBGs array sensors used as a reference is shown in Fig. 4.

The 1D reconstruction analysis was performed considering the last 15 s of the laser irradiation (45 to 60 s before switching the laser off, Fig. 4), close to the highest temperature increase and larger thermal gradient. This maximum temperature corresponds to 30 °C measured by the central grating of the 25-FBGs array (Fig. 5, green grating). The results obtained for the 1D temperature reconstruction are reported in Fig. 5. The temperature values provided by the Corning SMF-28 (GL = 5.2 mm) and the FBG sensors show a temperature difference > 10 °C in the central sensing points. Results for the Corning SMF-28 (GL = 1.2 mm) are not provided here because low GL value yielded to a low signal to noise ratio and it was not possible to measure any
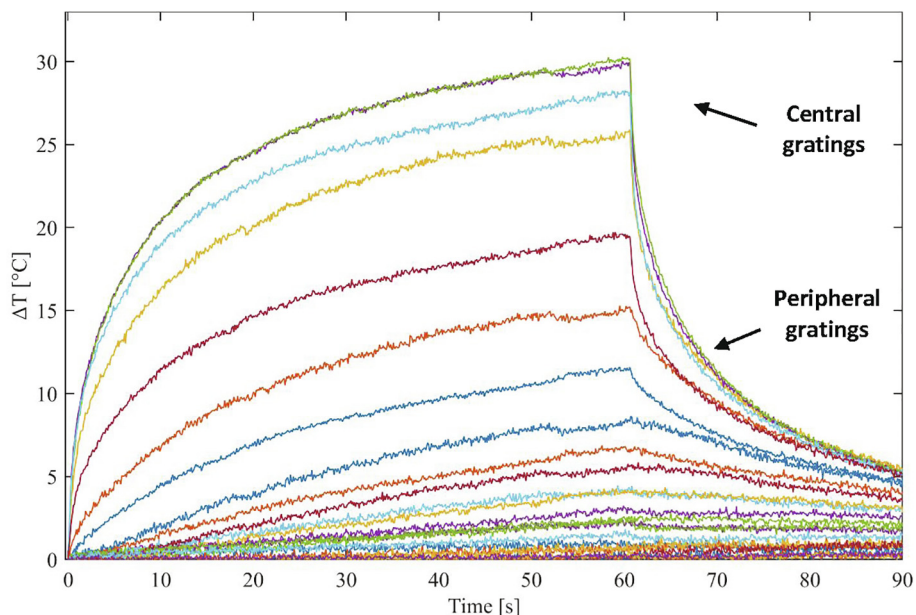
Fig. 4. Evolution of the temperature in time, measured by the 25-FBGs array sensor. Each line represents the signal provided by each grating.

temperature changes.

Temperature profiles measured with HD-FOS (GL = 5.2 mm and 1.3 mm) and FBG arrays are reported in Fig. 5b (for GL = 5.2 mm) and 5c (for GL = 1.3 mm). Also in this case, temperature distribution provided by LUNA HD-FOS is underestimated, due to the high GL value, and the difference with respect 25-FBGs array overcomes 15 °C. Conversely, GL = 1.3 mm allows for a smaller reconstruction error between the temperature curves measured from HD-FOS data and 25-FBGs array.

Table 1 lists the final values for RMSE and PD with corresponding standard deviations, obtained averaging among the considered time instants and tests. PD show positive values, thus demonstrating the 25-FBGs array better performances in retrieving maximum temperature

Table 1

Averaged RMSE and PD values obtained comparing 25-FBGs array with the other fiber optic sensors during the contactless ablation in the agarose phantom.

Sensors	RMSE [°C]	PD [°C]
10-FBGs array	1.1 ± 0.1	3.4 ± 0.3
Corning SMF-28 (GL = 5.2 mm)	7.1 ± 0.1	16.3 ± 0.3
HD-FOS (GL = 5.2 mm)	9.0 ± 0.2	22.6 ± 0.6
HD-FOS (GL = 1.3 mm)	2.1 ± 0.4	4.1 ± 1.4

peaks.

The SNR was computed for the FBGs arrays and the HD-FOS, both with GL = 5.2 mm and GL = 1.3 mm. Fig. 6 shows the evolution in
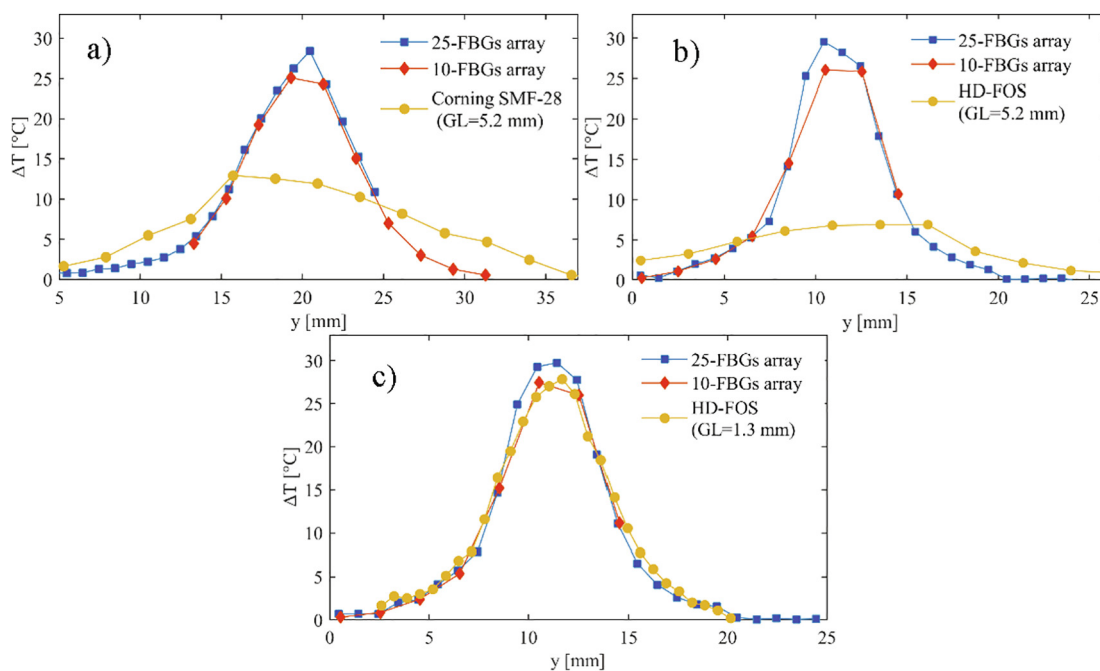

Fig. 5. Temperature distributions obtained at the end of ablation with the 25-FBGs array (blue line), the 10-FBGs array (red line) and with LUNA ODiSI-B sensor (yellow line): a) Corning SMF-28 (GL = 5.2 mm); b) HD-FOS (GL = 5.2 mm); and c) HD-FOS (GL = 1.3 mm). (For interpretation of the references to colour in this figure legend, the reader is referred to the web version of this article.)
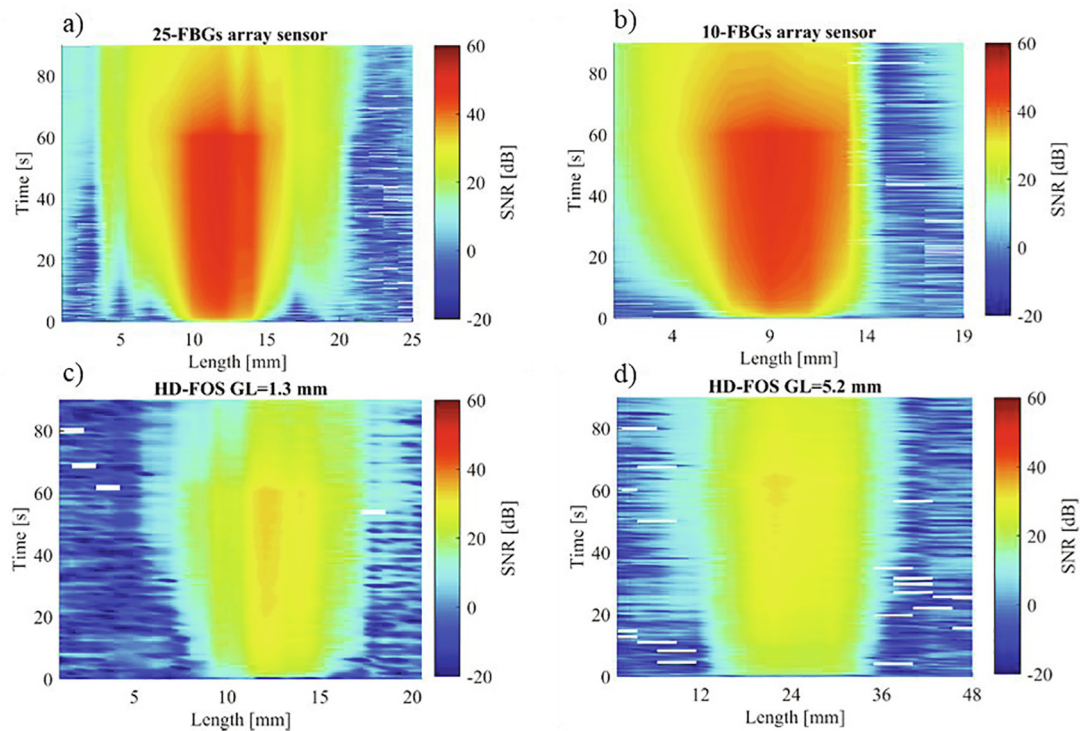
Fig. 6. SNR computed among time and length of a) 25-FBGs array sensor, b) 10-FBGs array sensor, c) HD-FOS with GL = 1.3 mm and d) HD-FOS with GL = 5.2 mm.

time of SNR evaluated among sensor length during the ablation procedure.

FBGs sensors provide larger values of SNR (maximum value of 50 dB, Fig. 5a and b) with respect the HD-FOS with GL = 1.3 mm (maximum SNR of 30 dB, Fig. 5c), even though they are subjected to a similar temperature signal; indeed the maximum temperature increase is 28 °C for both 10-FBG and HD-FOS (Fig. 4c). This evidence results from the larger noise contribution characterizing the distributed sensors. The poor spatial resolution of the HD-FOS, corresponding to GL = 5.2 mm, also affects the SNR values. Since the GL = 5.2 mm results into a maximum temperature difference of 22.6 °C with respect to the 25-FBGs array, also the SNR values over time are affected by the lower temperature values. The characteristic of the noise for each fiber optic sensor was assessed through the STD value of the measured temperature. Fig. 7 presents the STD for each grating of the arrays, in correspondence of the temperature increase (ΔT) detected by the sensing element subjected to the largest thermal gradient.

STD values are almost negligible for the FBGs sensors (Fig. 7a and b) at $\Delta T > 5$ °C. This result highlights that the SDT does not vary with the temperature change experienced by the agar phantom. A similar consideration can be done for HD-FOS with GL = 5.2 mm (Fig. 7d) at $\Delta T > 3$ °C. On the contrary, in the case of HD-FOS with GL = 1.3 mm (Fig. 7c), STD overcomes 1 °C for $\Delta T > 10$ °C, also following a random pattern along the sensing length. In all the graphs, the bottom part shows larger STD values because of the high thermal gradient generated in the first seconds of laser irradiation. The global view on the results in Figs. 5–7 lead to the assessment of the influence of the spatial resolution and grating lengths onto both the accuracy on the measured signal and the noise. When the gauge length in distributed sensors and grating length in FBG arrays tend to be the same, the two sensing systems show similar performances in terms of RMSE and PD. However, the analysis of both SNR and STD points out the best performances of the FBGs over the distributed sensors.

The measurements from the five triplets were processed to obtain a 2D temperature map on the agar gel surface (Fig. 8). Considering as a reference the 25-FBGs arrays map (T$_{max}$ 28 °C) in Fig. 8b, the poor spatial resolution for the Corning SMF-28 affect the final temperature

map (T$_{max}$ 12 °C). On the other hand, the lower sensing length and the better spatial resolution of the 10-FBGs array (Fig. 8c) allow a more accurate 2D temperature reconstruction (T$_{max}$ 26 °C). Moreover, 10-FBGs array spatial resolution lead to a slight underestimation, mostly for the high temperature values.

In general, the large GL value does not allow accurate temperature profile detection because of the high thermal gradient during LA. The use of GL = 1.3 mm significantly improves temperature measurements. Nevertheless, the 25-FBGs array has better performance than the HD-FOS sensor because of the smaller length of the sensing element (grating length = 0.9 mm vs. GL = 1.3 mm for HD-FOS) along which point temperature is measured. In addition, the 25-FBGs array shows good performances due to higher sensing length and higher resolution in comparison with the 10-FBGs array, i.e., 24 mm vs. 18 mm, and 1 mm vs. 2 mm, respectively.

4. Contact laser ablation of agarose phantom and *ex vivo* pancreas

The main objective of these experiments is to compare the temperature distribution provided by the 25-FBGs array and 10-FBGs array sensors during a contact ablation performed, firstly, in an agarose phantom and then for an *ex vivo* pancreas as well as reconstruct an accurate 3D temperature map in these two scenarios. Temperature spatial distribution data measured by 25-FBGs array were used as a reference for the analysis. RMSE between temperature curves and PD at fixed times were chosen, also in this case, for quantifying the error in temperature reconstruction for the 10-FBGs array sensor.

4.1. Material and methods

Contact ablation experiments were monitored with 4 arrays of 25 FBGs, 4 arrays of 10 FBGs arrays of 40 FBGs, simultaneously. The results obtained from the previous tests on the agar gel motivated the use of FBGs only. Each single FBG array was inserted from the upper part of the box through a rigid needle passing two opposite holes. The fiber laser was inserted 1.5 cm and 1 cm deep in the central hole for performing ablation in agar gel and pancreas, respectively (Fig. 9). The
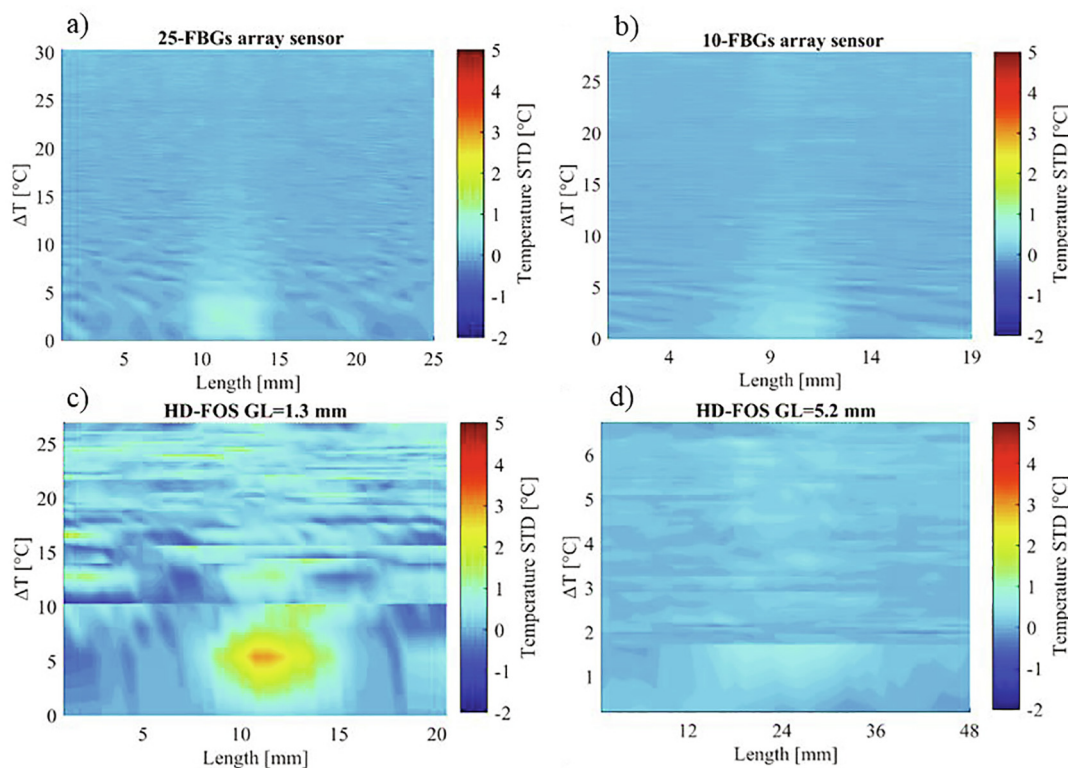
Fig. 7. Temperature Standard Deviation (STD) computed in function of the detected temperature increase (ΔT) among the length of a) 25-FBGs array sensor, b) 10-FBGs array sensor, c) HD-FOS with GL = 1.3 mm, d) HD-FOS with GL = 5.2 mm.
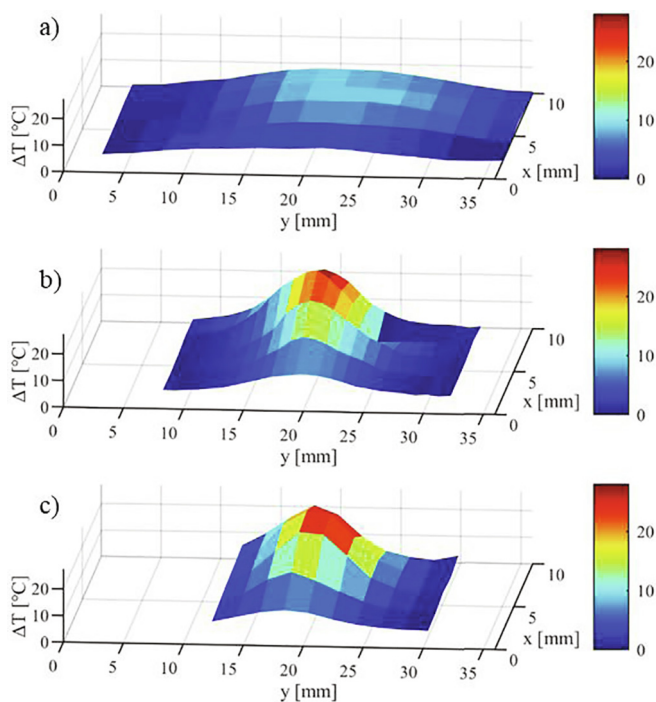

Fig. 8. Superficial Temperature maps at the end of the laser irradiation (60 s) considering non-interpolated data for: a) Corning SMF-28, b) 25-FBGs array c) 10-FBGs array.

sensing fibers were parallel to the laser tip, as schematized in Fig. 10. The 4 arrays of 25 FBGs were overlapped to the 4 arrays of 10 FBGs and placed at 2 mm distance from the laser (blue circle in Fig. 10). Three tests were performed for agarose phantom and *ex vivo* pancreas, respectively. In the agar gel experiments, the maximum temperature

increase of 12 ± 1 °C was reached for an ablation time of 60 s at 2 mm distance from the laser applicator. This temperature threshold was set in order to avoid agar gel melting in the laser tip proximity. Conversely, during the tissue ablation laser was tuned to reach a maximum temperature increase of 40 ± 1 °C in 120 s.

Two types of analysis were conducted: *i)* 1D comparison performed for the 4 pairs of overlapped arrays sensors (10-FBGs arrays and 25-FBGs arrays) at a 2 mm distance from the applicator. Hence, the lower is the distance from the applicator, the higher is the influence of sensors performances in temperature measurements [27]; *ii)* 3D map reconstruction considering data provided by the 25- and 40-FBGs arrays.

The four pairs of overlapped sensor arrays (25-FBGs and 10-FBGs), placed at laser top (T), bottom (B), right (R) and left (L) sides (Fig. 8) were aligned according to the approach explained for the 1D analysis (Section 3.1). Also in this case, RMSE and PD values were extracted in three time instants close to the end of the irradiation, and a mean was computed considering these results for the three experiments.

The 3D temperature map reconstruction was obtained thanks to the large number (420) of temperature points achieved with 8 arrays of 40-FBGs and 4 arrays of 25-FBGs. Temperature values for each FBG array were interpolated and a spatial alignment was computed for all the 12 arrays along *y* axis. After assigning a spatial position for each FBG array, 2D temperature maps at fixed *z* coordinates were obtained. Combination of 2D planes in the space enabled a 3D temperature map reconstruction.

4.2. Results and discussion

The results obtained for the 1D comparison for both agar gel and *ex vivo* pancreas are reported in Fig. 11.

Spatial resolution and sensing length of 10-FBGs array allow an accurate temperature reconstruction, especially in agarose phantom (Fig. 11a). Table 2 shows the average values and their standard deviations for RMSE and PD obtained averaging the results for each pair
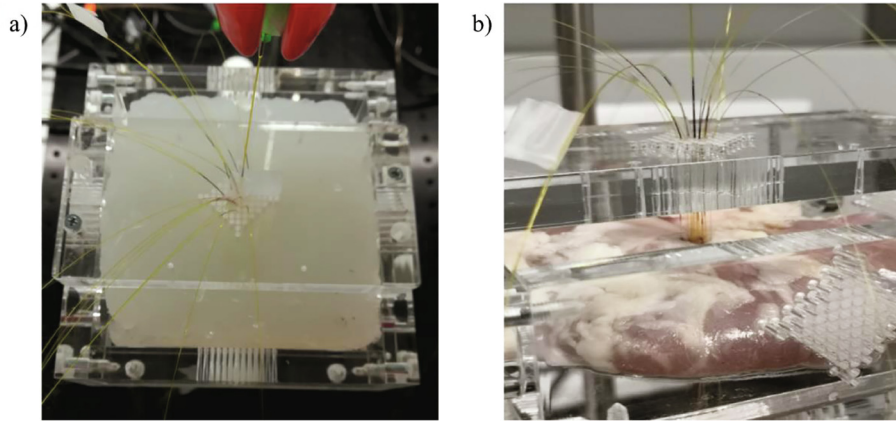
Fig. 9. Experimental setup for contact ablation in a) the agarose phantom and in b) the ex vivo pancreas placed inside the custom box. FBGs arrays inserted in the target thanks to the pattern of the box are visible.
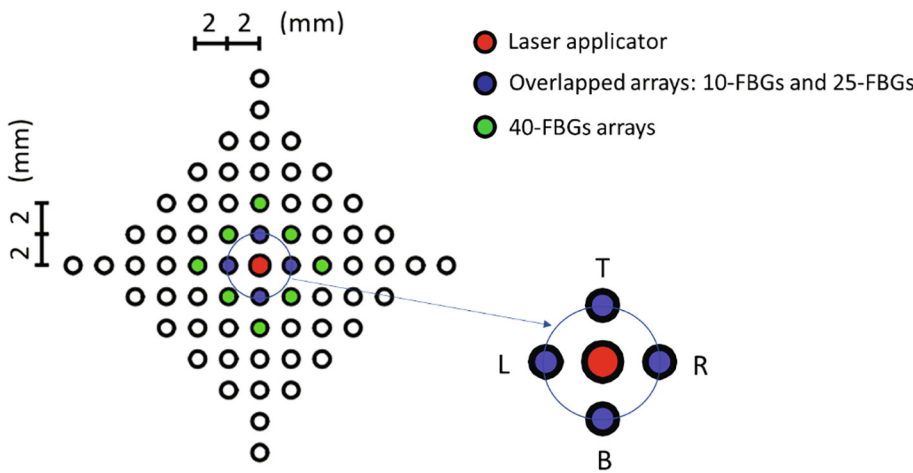

Fig. 10. Top view schematizing positions of laser applicator (red point), overlapped FBGs arrays (blue points) and remaining 40-FBGs array (green points) during the contact ablation experiments. Overlapped FBGs arrays' positions, top, right, left and bottom, are referred as T, L, R and B, respectively. (For interpretation of the references to colour in this figure legend, the reader is referred to the web version of this article.)

of overlapped sensors among the three experiments.

RMSE and PD parameters obtained for the pancreas show values slightly higher compared to data obtained for agar gel. Indeed, tissue inhomogeneities as well as the higher temperature gradient achieved can affect temperature profile accuracy when a low spatial resolution

for the FBGs is used. As in the contactless ablation case, PD show positive values thanks to better 25-FBGs array capabilities.

Figs. 12 and 13 show the 3D temperature map obtained during the agar gel and the *ex vivo* pancreas ablations, respectively. The performances of used FBGs allow for an accurate 3D temperature mapping.
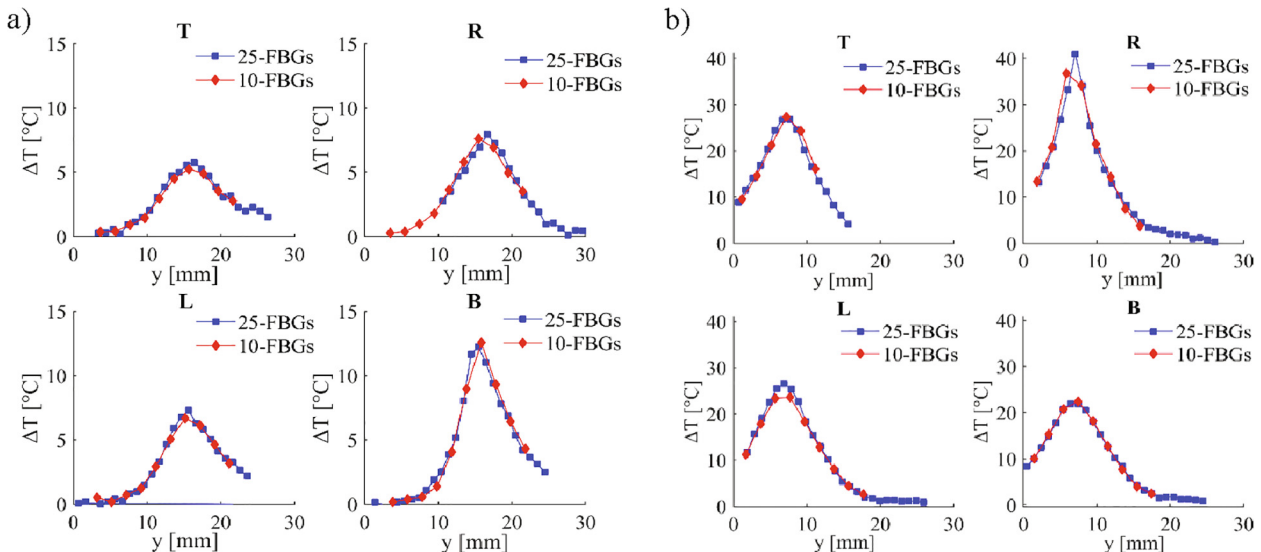

Fig. 11. Temperature distributions obtained at the end of ablation for the 4 positions (T, R, L, B) around laser tip during contact laser ablation in a) agarose phantom and b) ex vivo pancreas. Temperature profiles obtained with both 25-FBGs arrays and 10-FBGs arrays are shown.

Table 2
Average RMSE and PD values obtained comparing 25-FBGs array with 10-FBGs array during the contact ablation for both the tissue phantoms.

Position (ref to Figs. 10 and 11)	AGAR GEL PHANTOM		PANCREAS	
	RMSE [°C]	PD [°C]	RMSE [°C]	PD [°C]
Bottom	0.4 ± 0.1	0.1 ± 0.2	0.3 ± 0.03	0.01 ± 0.48
Left	0.3 ± 0.1	0.7 ± 0.2	1.2 ± 0.04	2.9 ± 0.2
Right	0.5 ± 0.1	0.6 ± 0.2	2.0 ± 0.1	5.5 ± 0.2
Top	0.2 ± 0.02	0.3 ± 0.2	1.0 ± 0.1	0.3 ± 0.2

Not symmetrical temperature distribution, visible also in 1D comparison (Fig. 11) is probably due to placement for laser applicator inside the media. Indeed, laser fiber was manually inserted from one hole, thus leading a non-perfect parallel position along y axis. Furthermore, in the case of the pancreas, tissue inhomogeneities can also contribute to the temperature spatial asymmetry.

From the results shown in Figs. 12 and 13 it is possible to compute the thermal gradient obtained for both agar gel phantom and pancreas.

The values of the thermal gradients observed at 2 mm and at 4 mm distance from laser applicator insertion point were computed over 5 mm-length and 1 mm-length, along the FBG longitudinal axis. Three experiments were repeated, and the final averaged values are reported in Table 3:

The results at 2 mm of distance from the laser applicator show a decrease of about 8 °C along 5 mm distance for the agarose phantom after 60 s from the start of irradiation. At the same time, the thermal

gradient along 5 mm measured in the pancreas is almost 27 °C, significantly decreasing at 4 mm distance. After 120 s results in the pancreas are similar to the ones obtained at 60 s, because the plateau of the temperature evolution was almost reached.

5. Discussion and conclusions

This study investigates the performances of fiber optic sensors in the reconstruction of an accurate spatial resolved temperature map in tissue phantoms undergoing laser ablation The 10-FBGs array and LUNA ODiSI-B with two types of fibers (standard Corning SMF-28® and HD-FOS provided by LUNA) in two modes (gage length = 1.3 mm and 5.2 mm) were compared with the 25-FBGs array (grating lengths 0.9 mm and edge-to-edge distance 0.1 mm). RMSE and PD values were measured to quantify a reconstruction error in different experimental configurations. In the agar gel contactless ablation, the 1D analysis highlighted that LUNA ODiSI-B using Corning SMF-28® does not provide an accurate temperature reconstruction: RMSE equal to 7 °C and a PD > 16 °C for $\Delta T_{max} \sim 28$ °C were obtained when longer gauge was used (GL = 5.2 mm). Also, with GL = 1.3 mm temperature reconstruction was not possible due to a small SNR value caused by high temperature gradient. On the other hand, LUNA ODiSI-B using HD-FOS with GL set to 1.3 mm has better performance: RMSE 2.1 °C and PD 4.1 °C at $\Delta T_{max} \sim 30$ °C were observed. SNR and temperature STD values further highlight the good performances of FBGs, providing $SNR_{max} \sim 50$ dB and STD < 0.5 °C. HD-FOS show $SNR_{max} \sim 30$ dB for both GL = 1.3 mm and GL = 5.2 mm, whereas the STD > 1 °C in the first case and STD < 0.5 °C in the second case. These results are determined by the larger noise affecting the signal when the resolution is
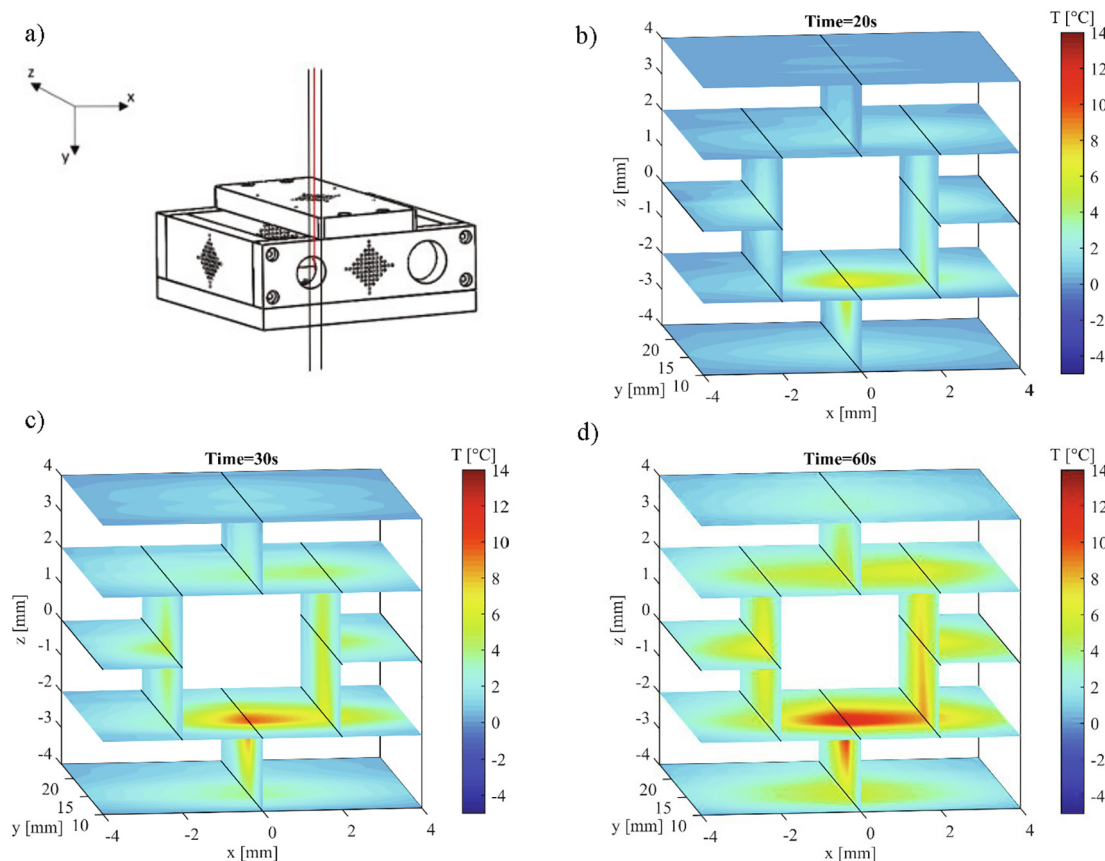

Fig. 12. Reconstructed temperature maps using 25-FBGs array and 40-FBGs array providing 420 sensing points during the agar gel ablation. Maps are extracted in three times: b) at the beginning of the irradiation (20 s), c) in the heating phase (30 s) and d) at the end of the irradiation (60 s). Black lines in the 2D planes represent the FBGs arrays. In a) a detail of the box (frontal view) showing the experimental setup orientation in accordance with the reference system. As example, only laser applicator (red line) and two FBGs fibers (black lines) are reported. (For interpretation of the references to colour in this figure legend, the reader is referred to the web version of this article.)
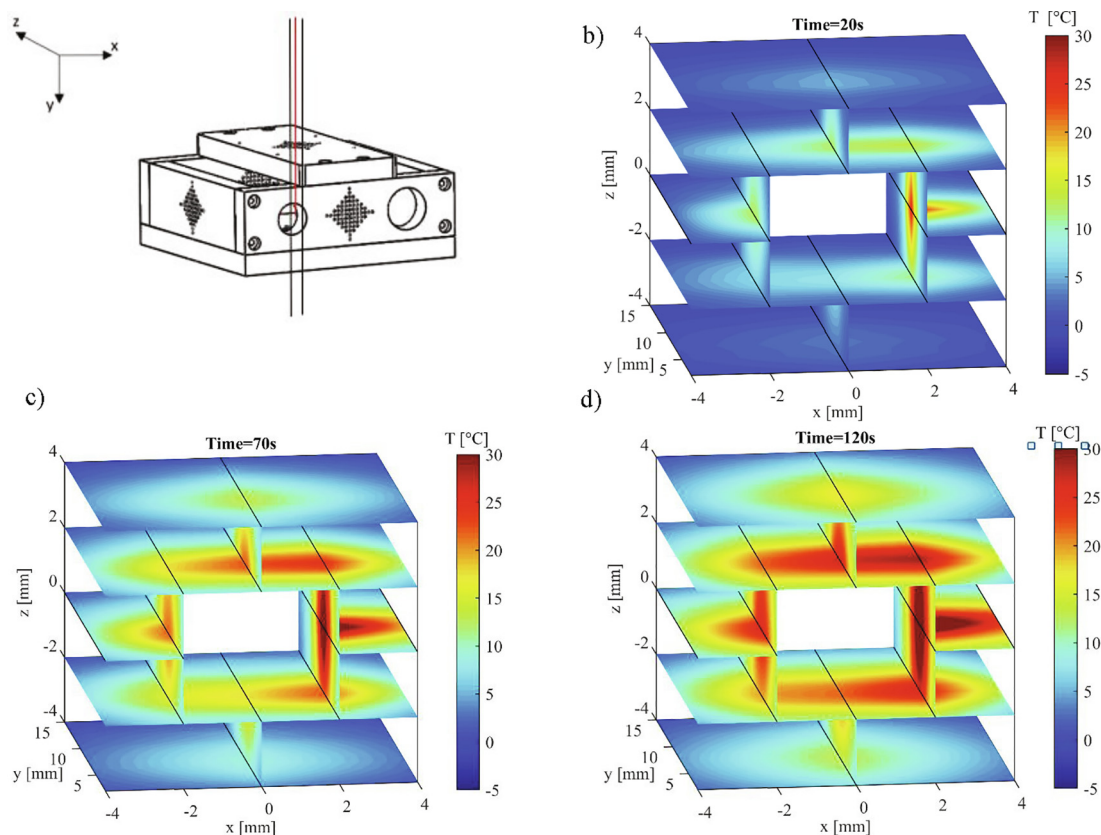
Fig. 13. Reconstructed temperature maps using 25-FBGs array and 40-FBGs array providing 420 sensing points during the ex vivo pancreas ablation. Maps are extracted in three times: b) at the beginning of the irradiation (20 s), c) in the heating phase (70 s) and d) at the end of the irradiation (120 s). Black lines in the 2D planes represent the FBG sensors. In a) a detail of the box (frontal view) showing the experimental setup orientation in accordance with the reference system. As example, only laser applicator (red line) and two FBGs arrays (black lines) are reported. (For interpretation of the references to colour in this figure legend, the reader is referred to the web version of this article.)

improved (GL = 1.3 mm), and by the lower signal provided in the opposite case (GL = 5.2 mm). According to these results, any improvement of spatial resolution for distributed sensors determines an increase of noise in the signal. Being both sensing features crucial for an accurate temperature measurement in media undergoing laser ablation, a trade-off could be insufficient for the specific application [38].

Concerning the 10-FBGs array performances, RMSE is ≤ 2.1 °C showing the lowest value of 0.3 °C when a $\Delta T_{max} < 15$ °C is reached in the agar gel contact ablation case. The highest PD is measured in the contact irradiation of the pancreas, where it achieves around 5.5 °C for $\Delta T_{max} \sim 40$ °C. The following results show that differences between the two FBG array types in terms of manufacturing and spatial resolution, lead to a difference in temperature distribution that can be considered negligible for the performed experiments. The temperature measured with 1 mm-spatially resolved FBGs array during contact laser ablation also allows an evaluation of the thermal gradient reached in pancreatic tissue. Close to the laser tip, a gradient of 7 °C/mm was measured in the pancreas after 1 min of ablation, and a decrease of almost 28 °C along 5 mm is registered. These results confirm the importance of a spatially resolved temperature sensing system in highly absorbing biological

media, particularly in *in vivo* cases, in which temperature above 100 °C and higher thermal gradient can be reached [15,39].

This investigation pointed out also that the use of one single fiber, even if with distributed sensing capability, holds a huge limit in providing a 3D temperature map reconstruction. Nanoparticles-doped optical fibers exhibiting enhanced scattering profiles have been proposed for temperature profile measurements across several fibers coupled to the LUNA system input [40]. However, the scanning rate of this method still need to be improved to allow a real-time sensing. On the contrary, multiplexing capability assured by FBG technology made the real-time measurement with 12 fiber optic sensors housing 420 sensing points (8 sensors with 40 gratings and 4 sensors with 25 gratings) possible in this bench test study. The ability to reconstruct an accurate real-time 3D temperature map is strongly dependent on the FBG array's configurations: the larger the number the better the resolution and the accuracy of the resulting map. In this regard, dense FBG sensors guarantee the best performances possible.

The experimental setup developed in this study is convenient for measuring temperature change in phantoms or *ex vivo* tissues. It allows a preliminary evaluation of sensors characteristics affecting on the

Table 3

Thermal gradient at 2 mm and 4 mm from the applicator insertion point; temperature variations are reported among 5 mm and 1 mm length.

Position	2 mm		4 mm	
Length	°C/5mm	°C/mm	°C/5mm	°C/mm
Agarose maximum gradient at 60 s from laser switched on	8.1 ± 0.2	0.8 ± 01	3.1 ± 0.1	0.3 ± 0.1
Pancreas maximum gradient 60 s from laser switched on	26.7 ± 0.3	7.2 ± 0.2	11.7 ± 0.3	1.1 ± 0.1
Pancreas maximum gradient 120 s from laser switched on	27.9 ± 0.2	7.3 ± 0.2	13.0 ± 0.1	1.1 ± 0.1

accuracy of the therapy control and of several therapy settings laser settings influencing the ablation outcome. Indeed, the assessment of performances of different fiber-optic based thermometers is the first step towards the definition of a strategy for accurate therapy control. In this perspective, the results achieved by this study are directly transferable into practical information for future preclinical or clinical studies.

CRediT authorship contribution statement

Federica Morra: Investigation, Data curation, Formal analysis, Writing - original draft. **Martina De Landro:** Conceptualization, Methodology, Writing - original draft. **Sanzhar Korganbayev:** Conceptualization, Software, Writing - original draft. **Alexey Wolf:** Resources. **Alexander Dostovalov:** Resources. **Alfredo Cigada:** Conceptualization, Writing - review & editing. **Paola Saccomandi:** Conceptualization, Writing - original draft, Writing - review & editing, Supervision, Funding acquisition.

Declaration of Competing Interest

The authors declare that they have no known competing financial interests or personal relationships that could have appeared to influence the work reported in this paper.

Acknowledgement

References

[1] A. Adam, L.M. Kenny, Interventional oncology in multidisciplinary cancer treatment in the 21st century, Nat. Rev. Clin. Oncol. (2015).

[2] A. Gillams, et al., Thermal ablation of colorectal liver metastases: a position paper by an international panel of ablation experts, the interventional oncology sans frontières meeting 2013, Eur. Radiol. (2015).

[3] T. de Baere, et al., Interventional oncology for liver and lung metastases from colorectal cancer: the current state of the art, Diagn. Interv. Imaging (2015).

[4] T. Gruber-Rouh, et al., Current strategies in interventional oncology of colorectal liver metastases, Br. J. Radiol. (2016).

[5] F.M. Di Matteo, et al., Feasibility of EUS-guided Nd:YAG laser ablation of unresectable pancreatic adenocarcinoma, Gastrointest. Endosc. (2018).

[6] P. Saccomandi, A. Lapergola, F. Longo, E. Schena, G. Quero, Thermal ablation of pancreatic cancer: a systematic literature review of clinical practice and pre-clinical studies, Int. J. Hyperth. (2018).

[7] A. Larghi, G. Rizzatti, M. Rimbaş, S. Crino, A. Gasbarrini, G. Costamagna, EUS-guided radiofrequency ablation as an alternative to surgery for pancreatic neuroendocrine neoplasms: who should we treat? Endosc. Ultrasound. (2019).

[8] G. Reddy, M.R. Dreher, C. Rossmann, B.J. Wood, D. Haemmerich, Cytotoxicity of hepatocellular carcinoma cells to hyperthermic and ablative temperature exposures: in vitro studies and mathematical modelling, Int. J. Hyperth. (2013).

[9] E. Schena, P. Saccomandi, Y. Fong, Laser ablation for cancer: past, present and future, J. Funct. Biomater. 8 (2) (2017) 19.

[10] R.J. Stafford, D. Fuentes, A.A. Elliott, J.S. Weinberg, K. Ahrar, Laser-induced thermal therapy for tumor ablation, Crit. Rev. Biomed. Eng. (2010).

[11] S. Tozburun, Superficial photothermal laser ablation of ex vivo sheep esophagus using a cone-shaped optical fiber tip, J. Biophoton. (2020).

[12] G. Quero, et al., Modular laser-based endoluminal ablation of the gastrointestinal tract: in vivo dose–effect evaluation and predictive numerical model, Surg. Endosc.

[13] R. Gassino, Y. Liu, M. Konstantaki, A. Vallan, S. Pissadakis, G. Perrone, A fiber optic probe for tumor laser ablation with integrated temperature measurement capability, J. Light. Technol. (2017).

[14] C.M. Pacella, L. Breschi, D. Bottacci, L. Masotti, Physical principles of laser ablation, Image-guided Laser Ablation (2020).

[15] Ashley J. Welch, Martin J.C. van Gemert (Eds.), Optical-Thermal Response of Laser-Irradiated Tissue, Springer Netherlands, Dordrecht, 2011.

[16] K.F. Chu, D.E. Dupuy, Thermal ablation of tumours: biological mechanisms and advances in therapy, Nat. Rev. Cancer 14 (3) (2014) 199.

[17] S. Ambastha, S. Pant, S. Umesh, V. Vazhayil, S. Asokan, Feasibility study on thermography of embedded tumor using fiber bragg grating thermal sensor, IEEE Sens. J. (2020).

[18] S. Korganbayev, et al., Detection of thermal gradients through fiber-optic Chirped Fiber Bragg Grating (CFBG): medical thermal ablation scenario, Opt. Fiber Technol. (2018).

[19] D. Tosi, E. Schena, C. Molardi, S. Korganbayev, Fiber optic sensors for sub-centimeter spatially resolved measurements: review and biomedical applications, Opt. Fiber Technol. 43 (March) (2018) 6–19.

[20] E. Schena, et al., Solutions to improve the outcomes of thermal treatments in oncology: multipoint temperature monitoring, IEEE J. Electromagn. RF Microwaves Med. Biol. (2018).

[21] E.G. Macchi, et al., Optical fiber sensors-based temperature distribution measurement in ex vivo radiofrequency ablation with submillimeter resolution, J. Biomed. Opt. (2014).

[22] G. Xin, et al., Distributed sensing technology of high-spatial resolution based on dense ultra-short FBG array with large multiplexing capacity, Opt. Express (2017).

[23] J. Xin, W. Zhuang, X. Lou, L. Zhu, M. Dong, High spatial resolution temperature field measurements by apodized short fiber Bragg grating sensors, Opt. Eng. (2019).

[24] P. Saccomandi, et al., Linearly chirped fiber Bragg grating response to thermal gradient: from bench tests to the real-time assessment during in vivo laser ablations of biological tissue, J. Biomed. Opt. (2017).

[25] D. Tosi, et al., Fiber-optic chirped FBG for distributed thermal monitoring of ex-vivo radiofrequency ablation of liver, Biomed. Opt. Express (2014).

[26] S. Korganbayev, et al., Thermal profile detection through high-sensitivity fiber optic chirped bragg grating on microstructured PMMA fiber, J. Light. Technol. (2018).

[27] P. Saccomandi et al., Influence of FBG sensors length on temperature measures in laser-irradiated pancreas: theoretical and experimental evaluation, in Proceedings of the Annual International Conference of the IEEE Engineering in Medicine and Biology Society, EMBS, 2013.

[28] D.K. Gifford, B.J. Soller, M.S. Wolfe, M.E. Froggatt, Distributed fiber-optic temperature sensing using Rayleigh backscatter, in: IET Conference Publications, 2005.

[29] E. Schena, D. Tosi, P. Saccomandi, E. Lewis, T. Kim, Fiber optic sensors for temperature monitoring during thermal treatments: an overview, Sens. (Switzerland) (2016).

[30] T. Erdogan, Fiber grating spectra, J. Light. Technol. 15 (8) (1997) 1277–1294.

[31] A.V. Dostovalov, A.A. Wolf, A.V. Parygin, V.E. Zyubin, S.A. Babin, Femtosecond point-by-point inscription of Bragg gratings by drawing a coated fiber through ferrule, Opt. Express 24 (15) (2016) 16232–16237.

[32] K.T.V. Gratten, B.T. Meggitt, Optical Fiber Sensor Technology: Volume 3: Applications and Systems, vol. 3. Kluwer Academic Pub, 1999.

[33] M. Froggatt, J. Moore, High-spatial-resolution distributed strain measurement in optical fiber with Rayleigh scatter, Appl. Opt. 37 (10) (1998) 1735–1740.

[34] L. Innovations, ODiSI-B Users Guide, 2017.

[35] LUNA datasheet. [Online]. Available: https://lunainc.com/wp-content/uploads/2018/10/LT_TD_EN-FY1403_TempCoeff_-40to200.pdf.

[36] J. Cho, B. Prasad, J.K. Kim, Near-infrared laser irradiation of a multilayer agar-gel tissue phantom to induce thermal effect of traditional moxibustion, J. Innov. Opt. Health Sci. (2018).

[37] R. Gassino, J. Pogliano, G. Perrone, A. Vallan, Issues and characterization of fiber Bragg grating based temperature sensors in the presence of thermal gradients, Meas. J. Int. Meas. Confed. (2018).

[38] L. Frich, Non-invasive thermometry for monitoring hepatic radiofrequency ablation, Minim. Invasive Ther. Allied Technol. (2006).

[39] S. Korganbayev et al., Highly dense FBG arrays for millimeter-scale thermal monitoring during nanocomposite-enhanced laser ablation, in: SPIE Photonics Europe, Optical Sensing and Detection VI, 2020.

[40] M. Jelbuldina et al., Multi-fiber distributed temperature profiling in ex vivo magnetite nanoparticle-mediated laser tissue ablation, in: Optical Interactions with Tissue and Cells XXXI, 2020, vol. 11238, p. 112380H.